Small Structures

small structures

www.small-structures.com

RESEARCH ARTICLE OPEN ACCESS

Multifunctional Sweat Sensors Using Semiconductor Fibers Based on Two-Dimensional Nanomaterials

Jun Hyun Park[1] | Jae Woo Park[2] | Min Seok Choi[1] | Sang Uk Pang[1] | Jun Seok Choe[1] | Tae Sang Yu[1] | Kyung-In Jang[1] | Jin-Tae Kim[3] | Ha Uk Chung[4] | Jang Hwan Kim[2,5] | Bong Hoon Kim[1,6,7,8]

[1]Department of Robotics and Mechatronics Engineering, DGIST, Daegu, Republic of Korea | [2]Department of Energy Systems Research, Ajou University, Suwon, Republic of Korea | [3]Department of Mechanical Engineering, Pohang University of Science and Technology, Pohang, Korea | [4]School of Biomedical Engineering, Korea University, Seoul, Republic of Korea | [5]Department of Materials Science and Engineering, Ajou University, Suwon, Republic of Korea | [6]Center for Physical AI, DGIST, Daegu, Republic of Korea | [7]TransHuman Robotics Research Center (Glocal Lab), DGIST, Daegu, Republic of Korea | [8]Global Bio-integrated Materials Center (Engineering Research Center), KAIST, Daejeon, Republic of Korea

Correspondence: Jin-Tae Kim (jimmy516@postech.ac.kr) | Ha Uk Chung (haukchung@korea.ac.kr) | Jang Hwan Kim (janghwankim@ajou.ac.kr) | Bong Hoon Kim (bonghoonkim@dgist.ac.kr)

Received: 19 December 2025 | **Revised:** 9 February 2026 | **Accepted:** 10 February 2026

Keywords: electrochemical sensing | fiber sensor | sweat sensors | wearable electronics

ABSTRACT

Sweat monitoring offers real-time insights into physiological conditions such as hydration, muscle fatigue, and metabolic status. However, conventional sweat sensors often face challenges associated with unstable skin contact and insufficient sampling. In this study, a fiber-based wearable sensing platform is proposed, which incorporates semiconducting molybdenum disulfide (MoS_2) and polylactic acid (PLA) composite fibers fabricated via wet spinning. By exploiting the high surface-to-volume ratio and n-type semiconducting nature of the MoS_2 network, the sensor selectively detects major biomarkers including electrolytes (Na^+ and K^+) and metabolites (lactic acid and NH_4^+) via distinct electrostatic screening and charge trapping mechanisms. Furthermore, the intrinsic capillary action and thermal insulation of the fibers ensured reliable sweat collection without the requirement for external power. Additionally, the composite fiber exhibits piezoresistive capabilities, enabling simultaneous pressure monitoring to track physical motion. Multifunctional sensing facilitates the early diagnosis of metabolic disorders and the precise tracking of athletic performance. The developed fiber-based sensor provides a robust textile-integrated solution for next-generation personalized healthcare monitoring.

1 | Introduction

Sweat, which originates from blood plasma, is a rich reservoir of biomarkers [1–4], including electrolytes (Na^+ and K^+) [5], metabolites (lactic acid, glucose, and ammonia) [6, 7], and proteins that serve as key indicators of physiological status [8, 9]. For instance, sweat sodium concentration offers vital insights into electrolyte loss and local ion transport, whereas potassium and ammonium ions have been explored as indicators of muscle ion homeostasis and metabolic stress, respectively. In addition to encompassing a comprehensive physiological profile, sweat analysis is gaining popularity as a diagnostic method owing to its inherent accessibility. Indeed, the noninvasive nature [10, 11] of sweat analysis represents a distinct advantage over traditional blood collection, rendering it a superior alternative for vulnerable populations [12, 13], including elderly individuals, patients at high risk of infection, and infants who are resistant to injections [14, 15]. Furthermore, continuous and real-time monitoring is possible since our bodies constantly produce sweat, even during routine daily activities [1, 16, 17]. Moreover, the ubiquitous availability of sweat across diverse epidermal sites facilitates its integration into wearable devices [18–22] in versatile forms. Consequently, sweat monitoring strategies are expected to hold considerable potential for a broad spectrum of

Jun Hyun Park, Jae Woo Park and Min Seok Choi contributed equally to this work.

applications, including clinical disease diagnostics, next-generation personalized healthcare [23], and sports science.

The operational fidelity of sweat monitoring systems depends on uninterrupted sweat sampling. However, sweat secretion rates fluctuate depending on individual activity levels and environmental conditions, posing a significant challenge to the consistent acquisition of sweat samples for analysis. Recently, substantial efforts have been devoted to developing sensing platforms that improve the stability of sweat sampling and sensing in daily life. For example, patch-type microfluidic systems [24–27] have enabled real-time monitoring of biomarkers such as lactate, proving valuable in sports science applications where large volumes of sweat are generated during intensive exercise [28]. Additionally, active sweat-induction strategies, including integrated Joule heating elements and iontophoretic stimulation [10], have enabled on-demand sampling in sedentary scenarios by leveraging external power sources and sophisticated circuitry [29–31]. While these platforms have excelled in their respective domains, intrinsic environmental and mechanical adaptability would [32] significantly facilitate their application in continuous daily sweat monitoring. Specifically, the capability to spontaneously retain body heat under ambient conditions and harvest minute fluid volumes is instrumental to preserving the sensing accuracy without the requirement for external power or vigorous physical exertion. Furthermore, achieving truly unobtrusive wearability implies replacing adhesive interfaces with a mechanically compliant design [33–35], ensuring universal comfort, even for users with delicate skin, such as the elderly or infants [36]. Consequently, a novel sweat-monitoring platform is required to enable reliable sweat sampling and efficient collection while guaranteeing superior comfort, even under sedentary conditions.

In this work, we developed a fiber-based wearable sweat-sensing platform that exploits semiconducting molybdenum disulfide (MoS_2)/polylactic acid (PLA) composite fibers with intrinsic thermofluidic capabilities. MoS_2 is a particularly attractive two-dimensional material because of its high surface-to-volume ratio, defect-mediated reactivity, and pronounced ionic gating behavior, which render it suitable for ionic and metabolite sensing in aqueous environments. Notably, the n-type semiconducting nature of the chemically exfoliated MoS_2 flakes facilitates the formation of ion-accessible active sites, enabling the detection of various biomarkers, including electrolytes and metabolites. Functional composite fibers are implemented via a wet spinning process to serve as the fundamental building blocks for the proposed monitoring platform. The intrinsic capillary action and thermal insulation of the fibers ensure reliable sweat collection without the requirement for external power, while flexible and adhesive-free design guarantees superior wearability. Beyond biochemical sensing, the piezoresistive response arising from the pressure-induced densification of the MoS_2 network is utilized to enable simultaneous physical motion tracking, thereby establishing a truly multifunctional sensing platform.

2 | Results and Discussion

2.1 | Overview of the MoS_2/PLA Composite Fiber Sensing Platform

The wearable sweat monitoring platform developed in this study was fabricated using semiconducting MoS_2 and PLA composite fibers. This fiber-based architecture was designed to ensure seamless epidermal integration, while the sensing platform is characterized by distinct functional attributes essential for reliable on-skin operation, as illustrated in Figure 1a. Specifically, a stable thermodynamic microenvironment is maintained due to the thermal insulation properties originating from the porous fiber structure, effectively minimizing heat dissipation and evaporation. Additionally, fluid transport is spontaneously achieved via intrinsic capillary action, ensuring spontaneous sweat uptake even under low-perspiration conditions. Furthermore, superior comfort and mechanical compliance are afforded by the flexible textile architecture, enabling noninvasive long-term wearability. Moreover, pressure sensing is enabled by the intrinsic piezoresistive response of the semiconducting MoS_2 network, allowing for the simultaneous detection of mechanical stimuli. The macroscopic processability inherent to the fibrous structure, which is exemplified by its capability for high-curvature deformation (<2.5 mm), allows the fabrication of versatile sensor configurations suitable for diverse applications that require sensing devices with various form factors, as demonstrated in Figure 1b. The fabrication of the composite fibers begins with the preparation of the precursor material, where bulk MoS_2 was electrochemically exfoliated to yield high-quality nanoflakes, which were subsequently dispersed to form a precursor solution (Figure 1c). The MoS_2 dispersion was then extruded using a wet-spinning system, generating continuous solid fibers within a coagulation bath, as illustrated in Figure 1d. Subsequently, an in-depth analysis of the resulting MoS_2/PLA composite fibers was systematically performed to evaluate their structural and chemical integrity. Morphological characterization via scanning electron microscopy (SEM) revealed a clearly defined porous structure, which is advantageous for interfacial sensing (Figure 1e). The compositional homogeneity within the matrix was identified by energy-dispersive X-ray spectroscopy (EDS), confirming the uniform spatial distribution of molybdenum, sulfur, carbon, and oxygen (Figure 1f). Additionally, the chemical states of MoS_2 within the composite fiber were analyzed using high-resolution X-ray photoelectron spectroscopy (XPS). As shown in Figure 1g, the Mo 3*d* spectrum exhibits a characteristic doublet originating from the semiconducting 2H phase, with Mo $3d_{5/2}$ and Mo $3d_{3/2}$ peaks located at ~229 and ~232 eV, respectively, confirming that the chemically exfoliated flakes largely retain their 2H crystal structure. A minor shoulder appearing at lower binding energies indicated the presence of a small fraction of the metallic 1T phase. This feature is commonly observed in electrochemically exfoliated MoS_2 and arises from cation intercalation and the accompanying electron injection during exfoliation, which induce a partial 2H → 1T lattice distortion. The metallic 1T component, although limited, introduces locally conductive pathways that support charge transport across the otherwise semiconducting MoS_2 network. Consequently, the mixed-phase composition contributes to stable electrical behavior while preserving the intrinsic surface reactivity required for ion-sensing interactions. This preserved material architecture facilitates multimodal sweat sensing and enables the selective discrimination of electrolytes (e.g., Na^+ and K^+) and metabolites (e.g., lactate and NH_4^+) based on distinct electrochemical interaction mechanisms, as discussed in the subsequent sections. The mixed-phase composition also underpins the stable electrical behavior essential for reliable sensor operation.

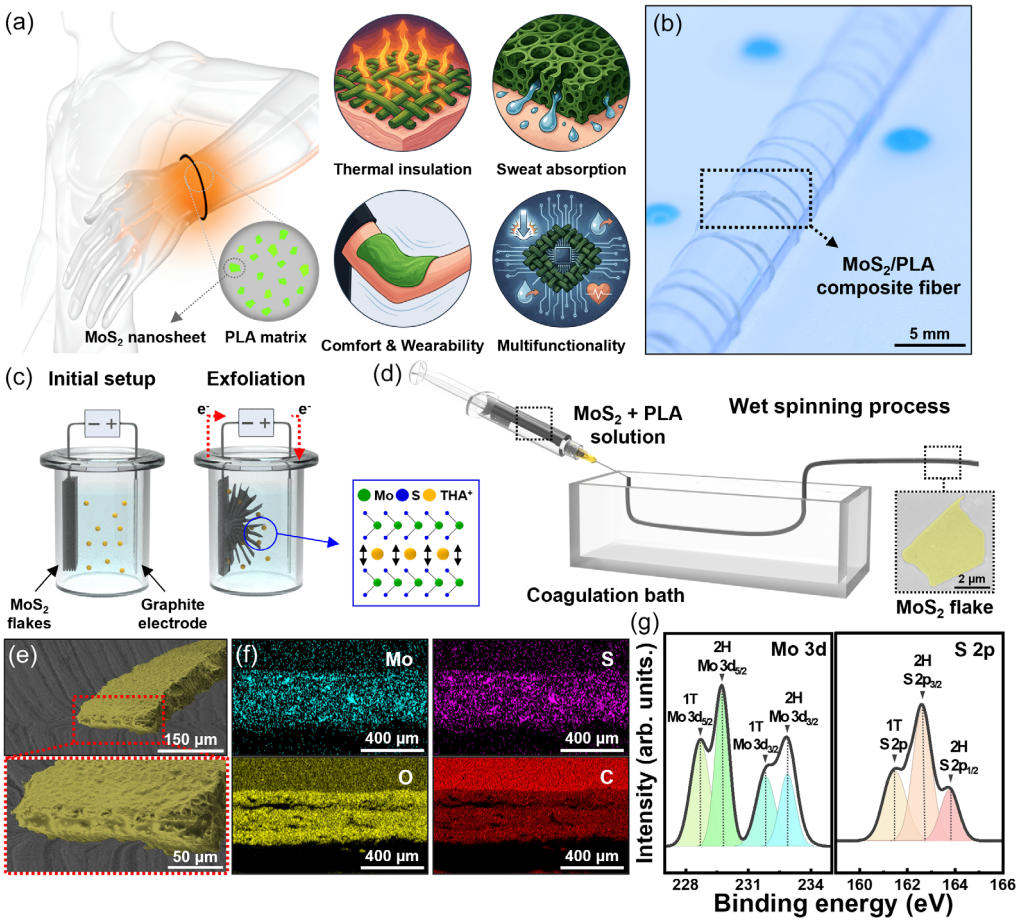

FIGURE 1 | Design, structure, and usage of the MoS_2/PLA composite fiber sweat sensor developed herein. (a) Schematic illustration highlighting the structural advantages and multifunctionality of a single MoS_2/PLA composite fiber sensor. (b) Conceptual photograph demonstrating the MoS_2/PLA composite fiber sweat sensor. (c) Schematic diagram depicting the electrochemical intercalation mechanism of ions into the MoS_2 layers. (d) Illustration of the wet-spinning process used to fabricate the MoS_2/PLA composite fibers. (e) SEM image showing the surface morphology of the fabricated fiber. (f) EDS elemental mapping revealing the distribution of constituent elements. (g) XPS spectra for the Mo 3*d* and S 2*p* components of the fabricated fibers.

2.2 | Resistive Sensing Mechanism for Ion Discrimination

The resistive sensing capability of the MoS_2/PLA composite fiber was demonstrated by characterizing its electrical properties upon interaction with representative biomarkers found in human sweat, including Na^+, K^+, NH_4^+, and lactate, as shown in Figure 2. In this setup, the MoS_2/PLA fiber is electrically connected through silver epoxy and silver wire, forming a stable two-terminal configuration that enables the direct monitoring of the current–voltage characteristics when exposed to external sweat droplets. The schematic illustration in Figure 2a highlights the structural arrangement of the fiber sensor and its conductive pathway, where the MoS_2 nanosheet network embedded along the fiber surface comes into direct contact with the incoming ionic solutions. The specific mechanisms governing these responses are shown in Figure 2b. Fundamentally, an electrically conductive percolation network was established by the arrangement of MoS_2 nanosheets. Upon exposure to an aqueous environment, the baseline resistance state (R_0) is determined by the electrochemical equilibrium at the interface, where the MoS_2 surface acquires a negative potential resulting from the deprotonation of surface defects and the specific adsorption of hydroxyl ions. Relative to this baseline equilibrium, the effective electrical conductivity exhibits divergent trends depending on whether electrolytes or metabolic biomarkers are present. When the sensor is exposed to small monovalent cations such as Na^+ and K^+, the MoS_2 surface primarily experiences weak electrostatic interactions because the strongly hydrated cations maintain their solvation shells and interact only at the outer-sphere level. This leads to the accumulation of hydrated ions near the MoS_2 interface and the formation of an electric double layer (EDL) [37, 38]. The resulting interfacial EDL potential modulates the carrier density through field-effect gating, increasing electron accumulation at the channel surface without invoking chemical doping [39]. Conversely, metabolic biomarkers such as NH_4^+ and lactate exhibit strong specific interactions with the MoS_2 surface. NH_4^+ tends to reduce the effective electron density through interfacial hydrogen bonding or electrostatic interactions with hydroxylated or partially oxidized sites on the MoS_2 surface. Similarly, lactic acid perturbs the interfacial charge distribution through dipolar interactions originating from its functional groups (e.g., carboxyl and hydroxyl moieties) or defect-assisted localization, which effectively lowers the apparent electron density. These specific interactions (i.e., carrier scattering and charge modulation) collectively suppress electron mobility and reduce the free carrier concentration, thereby decreasing the overall electrical conductivity.

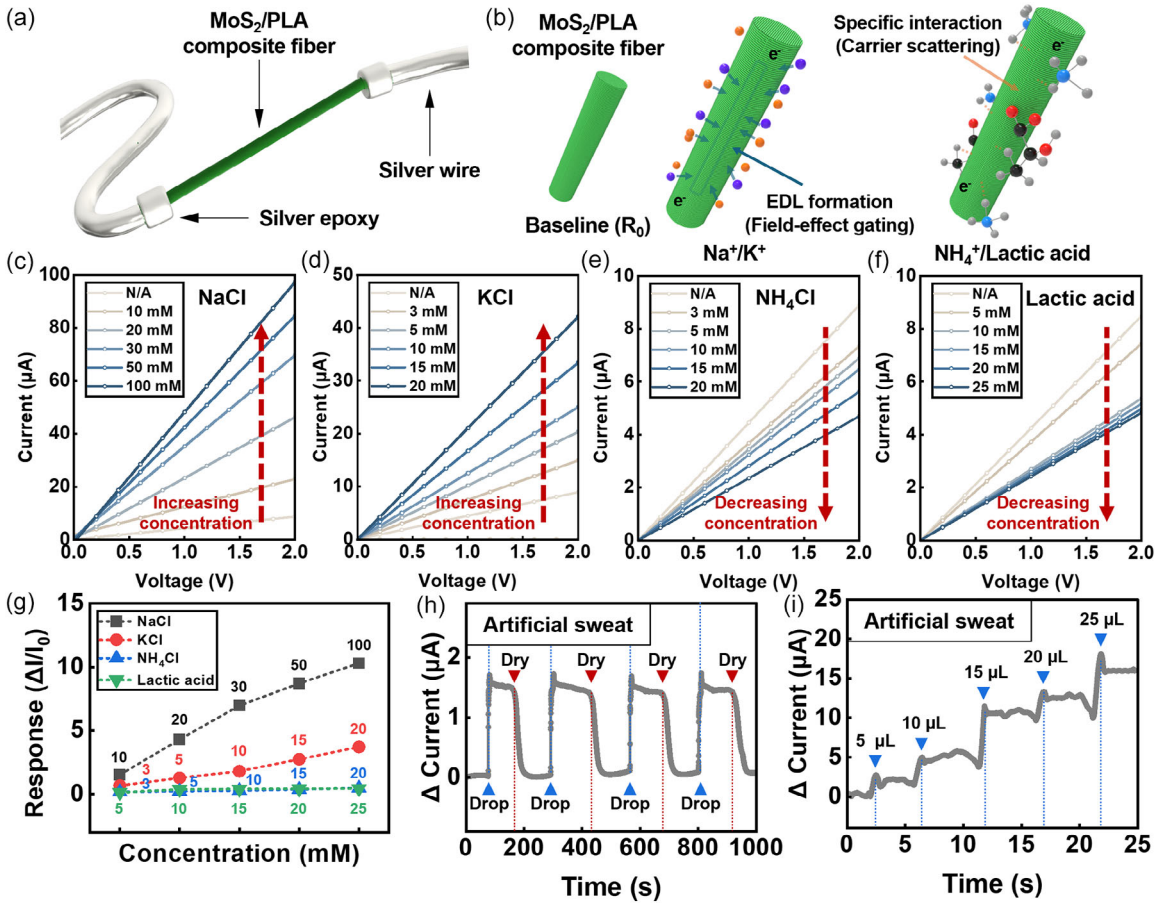

FIGURE 2 | Chemiresistive sweat sensing performance of the developed fiber sensor. (a) Schematic diagram illustrating the fabrication process of the single MoS_2/PLA composite fiber sweat sensor. (b) Schematic illustration of the sensing mechanisms, depicting electric double-layer formation for ions (Na^+, K^+) and charge-trapping effects for NH_4^+ and lactic acid. (c–f) *I–V* curves measured under varying concentrations of (c) NaCl, (d) KCl, (e) NH_4Cl, and (f) lactic acid. (g) Comparative response plot showing the relative current changes as a function of the analyte concentration. (h) Real-time current monitoring of the sensor response to artificial sweat. (i) Current variations observed with respect to different volumes of artificial sweat.

The current–voltage (*I–V*) curves recorded measured under varying concentrations of NaCl, KCl, NH_4Cl, and lactic acid are presented in Figure 2c–f, where the slopes represent the effective electrical conductivity. In the NaCl and KCl solutions, the conductivity increased linearly with increasing ionic concentration, confirming the dominance of the EDL gating effect. In contrast, increasing concentrations of NH_4Cl and lactic acid induced a monotonic decrease in conductivity, confirming the prevalence of carrier scattering and charge trapping effects. These contrasting electrical behaviors depending on the ionic species, which were further validated by the normalized current trends shown in Figure 2g, provide foundational evidence that the single-fiber sensor can perform chemical discrimination based on the distinct directional response and magnitude of the resistive signal. Analytical metrics extracted from concentration-dependent measurements further supported robust quantification (Figure S2). The normalized response ($\Delta I/I_0$) exhibited a linear dependence on analyte concentration over the tested ranges of 0–100 mM (NaCl), 0–20 mM (KCl), 0–20 mM (NH_4Cl), and 0–25 mM (lactic acid), with high linearity ($R^2 = 0.984–1.000$). The corresponding slopes quantitatively capture the opposite trends for electrolytes versus metabolites, and the estimated limits of detection remained well below the lower bounds of the tested ranges, ensuring reliable resolution of physiological concentration changes. Notably, these opposing electrical trends enable the direct discrimination of metabolic biomarkers from electrolytes, eliminating the requirement for complex calibration or signal processing. A comparative overview of recently reported MoS_2- and fiber-based sweat sensing platforms is provided in Table S1 to highlight the distinctive features of the proposed MoS_2/PLA composite fiber [40–45].

To evaluate the sensor under sweat-relevant chemical complexity, we measured electrical responses in mixed electrolyte and electrolyte–metabolite systems (Figure S3). Electrolytes produced positive responses, whereas metabolites produced negative responses, and these signatures were preserved in mixtures, showing an approximately linear trend within the tested physiological range. Consistent with this behavior, NaCl and KCl showed positive concentration-dependent sensitivities, while lactic acid exhibited an opposite (negative) sensitivity.

To assess practical reliability, we examined stability across the physiological pH range (4.0–7.5) and under standard sweat conditions. Although MoS_2 can exhibit pH-dependent electrical behavior, these effects are intensely screened under the high ionic strength conditions typical of sweat (10–100 mM), where H^+ is comparatively negligible. Experimentally, *I–V* characteristics measured in a 45 mM NaCl background and in a sweat-mimicking mixture (with glucose and urea) showed minimal variation with pH or

coexisting substances (Figure S4), confirming robust selectivity and interference suppression in sweat-relevant environments.

Subsequently, the long-term reliability and reusability of the developed fiber sensor were verified through cyclic transitions between "Drop" and "Dry" states, as shown in Figure 2h. The observed consistent signal recovery to the baseline confirms robust reversibility, ensuring sustainable sensing performance even under repetitive operational stresses, such as prolonged wear and washing cycles. Furthermore, the capillary-driven sweat absorption and real-time monitoring capabilities facilitated by the fibrous architecture were quantified by the sequential addition of microvolume droplets. In addition, the excellent durability and stability of the sensor were confirmed through repeated measurements (Figure S5) and a 1-month long-term storage test (Figure S6). As presented in Figure 2i, the sequential addition of 5 μL droplets induced an immediate stepwise increase in current, facilitated by spontaneous capillary uptake. The resulting rapid signal elevation with negligible latency indicates efficient liquid transport along the fiber surface, in contrast to the typical stagnation observed in static droplets. Thus, successful μL-scale detection confirms that the enhanced capillary action of the composite fiber effectively addresses the critical challenge of securing sufficient sample volumes in low-perspiration scenarios. Stable stepwise responses persisted up to a cumulative volume of 25 μL without signal saturation, demonstrating reliable μL-scale sampling without external pumping or power assistance.

2.3 | Electrochemical Capacitive Sensing Performance

The electrochemical capacitive sensing performance of the developed sensor was subsequently demonstrated using a three-electrode system, in which the MoS_2/PLA composite fiber served as the working electrode (WE), a platinum wire as the counter electrode (CE), and Ag/AgCl as the reference electrode (RE), as illustrated in Figure 3a. The underlying capacitive mechanism involving ion dynamics is schematically depicted in Figure 3b and comprises two distinct phases, namely, forward and reverse scanning (charge and discharge, respectively). Specifically, during the forward scan (charging), the application of an electric potential polarizes the fiber surface, inducing the electromigration and accumulation of counter-ions from the electrolyte to establish a dense EDL. Additionally, during the reverse scan (discharging), reversing the potential sweep direction triggers ion desorption and releases the stored interfacial charge. The current observed in cyclic voltammetry (CV) profiles originates from this continuous flux of physical adsorption and desorption and is quantified as capacitance ($C = \frac{Q}{\Delta V}$). Consequently, a larger CV

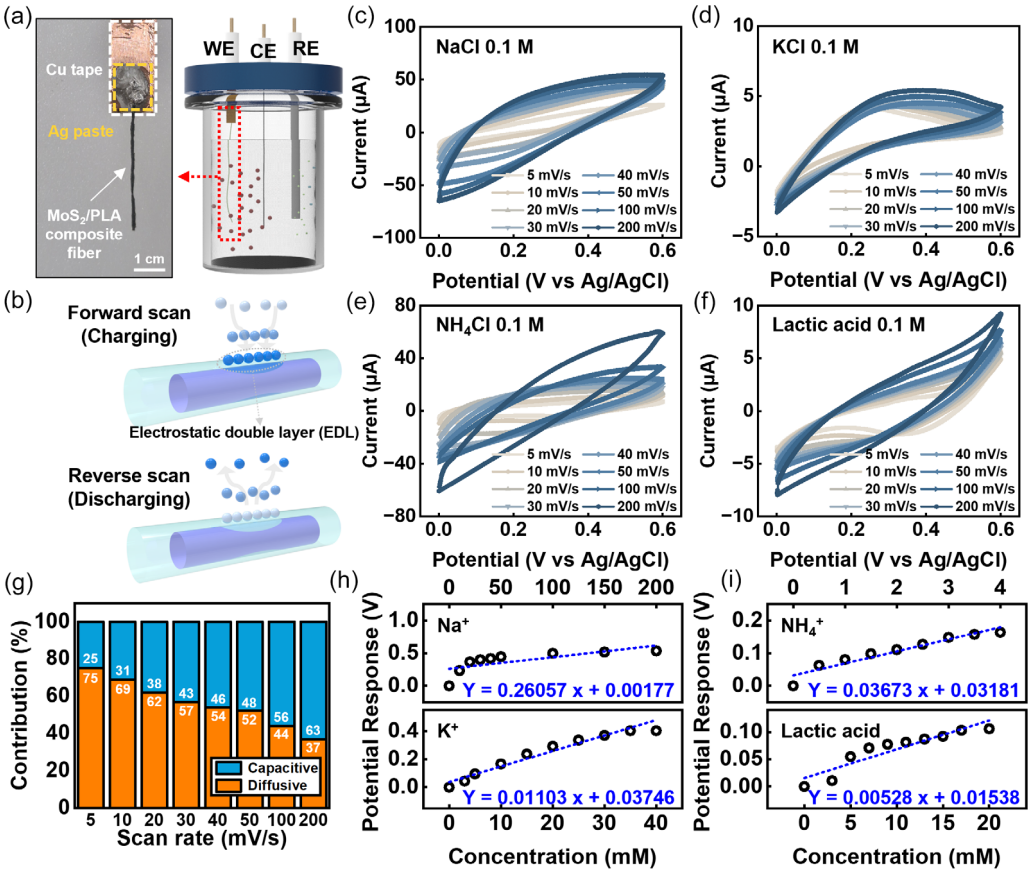

FIGURE 3 | Electrochemical sensing properties and ion detection performance of the developed sensor. (a) Schematic illustration and optical image showing the design of the fiber-based ion sensor and the experimental setup for electrochemical measurements. (b) Schematic diagram elucidating the electrochemical sensing mechanism and ion interactions at the interface. (c–f) CV curves measured under varying concentrations of (c) NaCl, (d) KCl, (e) NH_4Cl, and (f) lactic acid. (g) Analysis of the capacitive contribution of the fiber sensor as a function of scan rate. (h,i) Calibration plots and linear regression analysis indicating the sensitivity slopes for (h) NaCl and KCl and (i) NH_4Cl and lactic acid.

hysteresis loop signifies enhanced ion adsorption capacity, which directly correlates with enhanced sensitivity. Subsequently, CV curves were measured at various scan rates (from 5 to 200 mV/s) to analyze the charge storage behavior, as shown in Figure 3c–f. The fiber electrode exhibited quasirectangular CV profiles devoid of distinct oxidation/reduction peaks across all target analytes (NaCl, KCl, NH_4Cl, and lactic acid), confirming that the sensor operation is predominantly governed by the electric double-layer capacitance (EDLC) rather than Faradaic reactions. Notably, the current increased proportionally with the scan rate, demonstrating excellent rate capability. Although the overall charge storage followed EDLC behavior, the magnitude of ion accumulation remained strongly dependent on the specific ion–MoS_2 interfacial interactions shown in Figure 2, which modulate both the resistive and capacitive responses.

The charge storage kinetics were quantitatively analyzed by deconvoluting the total current into surface-controlled (capacitive) and diffusion-controlled contributions, as shown in Figure 3g. The resulting analysis revealed a mixed charge storage mechanism. While diffusive processes prevailed at lower scan rates (75% contribution at 5 mV/s), the capacitive contribution progressively increased, reaching 63% at 200 mV/s. This transition suggests that a high surface-to-volume ratio facilitates rapid surface ion adsorption at high operating speeds. Furthermore, the ion discrimination capability was assessed by measuring the open-circuit potential (OCP) response, as shown in Figure 3h,i. In contrast to Na^+ and K^+ (Figure 3h), whose OCP shifts are dominated by electric double-layer formation, the OCP responses to NH_4^+ and lactic acid shown in Figure 3i arise from specific interfacial interactions with the MoS_2 surface. Hydrogen bonding, dipolar interactions, and defect-assisted adsorption perturb the local interfacial charge distribution, resulting in concentration-dependent OCP shifts. A linear potential response was observed with increasing concentrations of Na^+ and K^+, wherein the sensitivity (slope) for K^+ (0.261 V/mM) was ~23 times higher than that for Na^+ (0.011 V/mM). This difference in sensitivity highlights the potential for selective ion discrimination without the requirement for additional ion-selective membranes.

2.4 | In Vivo Demonstration and Real-World Application of the Fiber Sensor Platform

To demonstrate the practical applicability of the developed MoS_2/PLA composite fiber, its performance was examined under real-world conditions, emphasizing the inherent reliability enabled by the fibrous architecture. Figure 4a,b demonstrates the thermal insulation capability achieved when the composite fiber was integrated into a ring-type wearable device. Owing to the multilayered porous structure of the fiber bundle, which naturally traps air between filaments, the assembled ring creates a localized warm microenvironment at the skin–sensor interface, helping retain naturally secreted perspiration by reducing evaporative cooling, rather than inducing additional sweat production. After placing the ring-based sensor on the subject's finger (Figure 4a), infrared

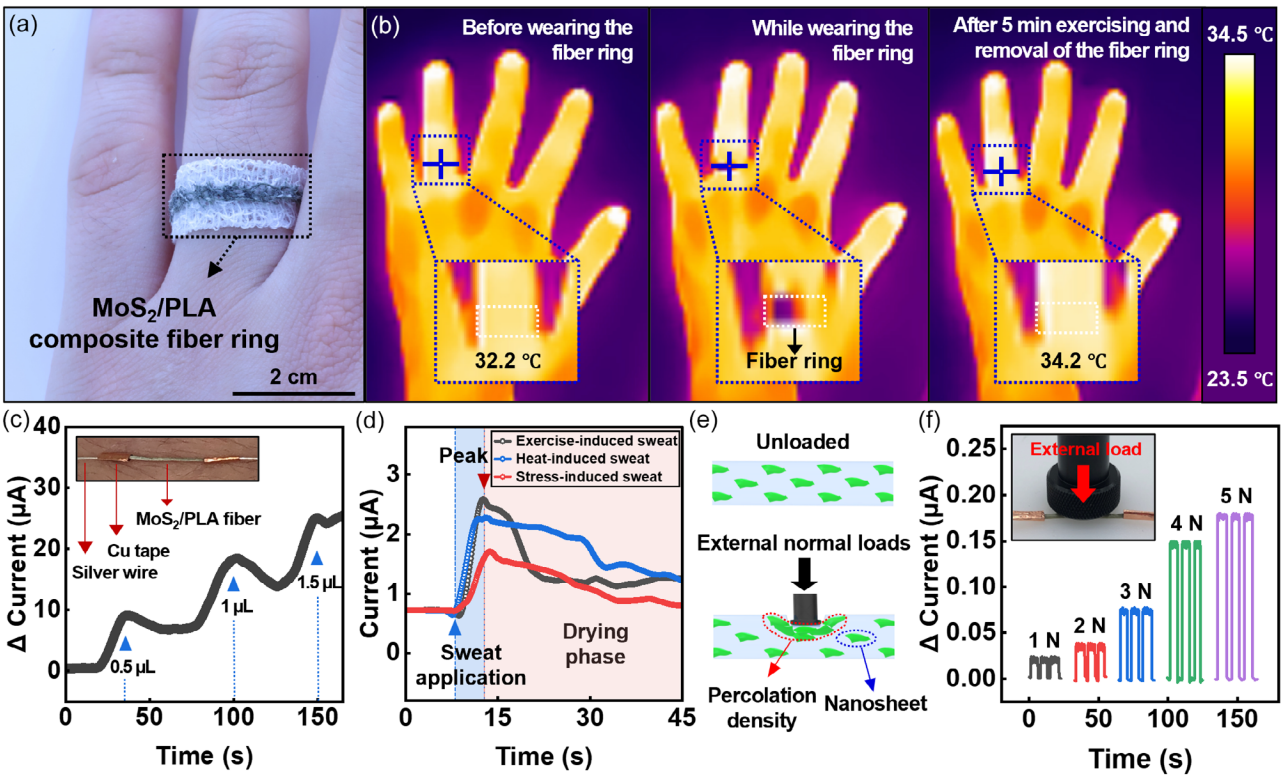

FIGURE 4 | Real sweat response and demonstration of sensor application in multifunctional wearable electronics. (a) Photographic image of the ring-shaped fiber sensor worn on a finger for real-time temperature monitoring applications. (b) Infrared (IR) camera images monitoring skin temperature variations in different situations: (i) before wearing the fiber ring, (ii) while wearing the fiber ring, and (iii) after removing the ring following 5 min of exercise. (c) Plot showing variations in current relative to the volume of sweat. The inset presents a photographic image of the MoS_2 fiber sensor. (d) Real-time current response variations recorded under three different human conditions. (e) Schematic illustration of the pressure sensing mechanism. (f) Real-time current response of the sensor subjected to cyclic external pressure loads ranging from 1 to 5 N.

thermography (Figure 4b) verified that the covered skin region maintained a noticeably higher and more stable temperature than the surrounding uncovered area. Additionally, the MoS_2/PLA composite fiber exhibited passive, capillary sweat uptake owing to its fibrous structure. As shown in Figure 4c, the sensor demonstrated excellent microvolume detection. In this configuration, the MoS_2/PLA fiber was electrically connected at both ends using Cu tape, which was further connected to silver wires (inset, Figure 4c), forming a stable two-terminal measurement configuration. The sequential deposition of small droplets (0.5, 1.0, and 1.5 μL) produced clear, stepwise increases in current, confirming rapid capillary uptake and sensitive transduction at the MoS_2–electrolyte interface.

Figure 4d demonstrates the ability of the developed sensor to discriminate between different physiological states depending on their unique perspiration profiles. When tested under exercise-, heat-, and stress-induced conditions, the fibers exhibited distinct temporal signatures, including differences in onset time, peak magnitude, and decay behavior. These results indicate that, even under low perspiration and high fluctuation conditions, the sensor can reliably distinguish between physiological states based on subtle variations in early sweat onset and transient signal behaviors. In addition to its biochemical sensing capability, the composite fiber also functions as a mechanical sensor, as shown in Figure 4e, which illustrates that the application of an external load compresses the MoS_2/PLA fiber and increases the overlap density of adjacent MoS_2 nanosheets. This densification of the percolation network reduces the electrical resistance, yielding a clear piezoresistive response [46, 47], as the pressure-induced signal originates from changes in the conductive pathways rather than from charge generation. Figure 4f provides quantitative pressure-response data, wherein it can be seen that stepwise loads ranging from 1 to 5 N generate distinct and reversible changes in current (ΔI). As shown in the inset of Figure 4f, these forces were applied using a motorized test stand equipped with a force gauge, enabling precise and reproducible force application during the measurements. In addition, after repeated bending–release cycles, the MoS_2/PLA composite fiber showed negligible permanent resistance change in the steady state, with a normalized variation of less than 0.7% after 500 cycles at a minimum inner curvature radius of ~2 mm (Figure S7). Consistent with this mechanical robustness, the fiber was confirmed to respond to a pressure of 10 N and function properly under repetitive pressure at 5 N, which is the pressure level typically applied to fabrics in daily life (Figure S8). Collectively, these on-skin and bench-top experiments demonstrate the ability of the MoS_2/PLA composite fiber to support stable and reliable multimodal sweat sensing, including microvolume sweat collection and physiological-state tracking, while its additional piezoresistive response enables multifunctional on-body monitoring with simultaneous mechanical sensing.

3 | Conclusion

This work presents a fiber-based wearable sweat sensor composed of semiconducting MoS_2 and PLA composite fibers fabricated via wet spinning. Superior comfort and wearability were achieved through its textile-integrated architecture, enabling stable skin contact and consistent sampling capabilities, even in sedentary scenarios. The intrinsic thermal insulation and capillary action of the fiber architecture facilitated passive sweat induction and efficient sweat collection without the requirement for external power, thereby ensuring a reliable sensing environment. Precise multifunctional sensing was achieved by exploiting the high surface-to-volume ratio and n-type semiconducting nature of the MoS_2 network. Additionally, distinct electrochemical interaction mechanisms allowed for the selective discrimination of biomarkers; electrostatic screening effects enhanced the conductivity in the presence of electrolytes (i.e., Na^+ and K^+), whereas charge trapping and scattering effects dominated the response to metabolites (i.e., NH_4^+ and lactic acid). Furthermore, the fibers exhibited exceptional mechanical stability under nonlinear deformation, ensuring signal integrity during dynamic physical movement. Simultaneously, the pressure-induced piezoresistive response of the MoS_2 network enabled physical motion tracking, demonstrating multifunctionality. These findings underscore the potential of MoS_2/PLA composite fibers as a robust, textile-integrated solution for next-generation personalized healthcare monitoring, with anticipated impacts extending beyond sensors, biomedical engineering, and sports science to the broader wearables industry, including garment applications.

4 | Experimental Section

4.1 | Electrochemical Exfoliation of the MoS_2 Nanosheets

A thin piece of a freshly cleaved bulk MoS_2 crystal was employed as the cathode, while a graphite rod served as the anode. The electrolyte solution was prepared by dissolving tetraheptylammonium bromide (THAB; $d \approx 20$ Å, Sigma–Aldrich) and polyvinylpyrrolidone (PVP; $M_w = 40{,}000$, Sigma–Aldrich) in *N*,*N*-dimethylformamide (DMF) at concentrations of 5 and 20 mg/mL, respectively. The intercalation reaction was performed at a constant voltage of 4 V for ~3 h. During this process, the bulk crystals expanded significantly and disintegrated into smaller fragments, which settled at the bottom of the vial. Upon completion of the reaction, the intercalated material was collected and transferred to fresh PVP/DMF solution (20 mg/mL), followed by bath sonication for 10 min. To isolate the MoS_2 nanosheets, the resulting dispersion was subjected to centrifugation at 3 000 rpm for 30 min to remove the unexfoliated bulk particles. The supernatant was then collected and subjected to centrifugation at 15 000 rpm for 30 min. The washing step was repeated to obtain the pure nanosheets.

4.2 | Fabrication of MoS_2/PLA Composite Fibers via Wet Spinning

The spinning dope was prepared by dissolving biodegradable PLA ($M_w \approx 60{,}000$, Sigma–Aldrich) in a preheated MoS_2 dispersion (0.3 wt%). The resulting mixture was maintained at 60°C under continuous stirring to ensure complete polymer dissolution and the homogeneous distribution of the MoS_2 nanosheets within the matrix. The final concentration of the MoS_2–PLA spinning dope was adjusted to 10 wt% to achieve the optimal viscosity for spinning. The composite fibers were fabricated via wet spinning using a customized slit nozzle. The nozzle was prepared by mechanically flattening the tip of a standard cylindrical needle to create a slit-like opening designed for the fabrication of flat fibers. The prepared dope was extruded at a controlled flow rate

of 0.1–0.2 mL/min in a coagulation bath composed of ethyl acetate and hexane (1:1, v/v). Upon contact with the nonsolvent mixture, the extruded jet rapidly solidified due to solvent exchange. Finally, the solidified fibers were collected on a rotating drum at winding speeds of 1–20 cm/s.

4.3 | Structural and Surface Characterization

The morphology of the fabricated fibers was analyzed using field-emission SEM (FE-SEM; Hitachi Su-8000, Hitachi High-Tech). The spatial distribution of the elements was visualized via EDS using a Hitachi SU8230 system (Hitachi High-Tech). To investigate the surface chemical states, the MoS_2/PLA composite fibers were subjected to XPS (K-Alpha+, Thermo Fisher Scientific), and a comparison was performed with bulk MoS_2 crystals.

4.4 | Electrical and Electrochemical Sensing Measurements

To evaluate the electrical properties of the developed sensor, copper tape and conductive silver paste were applied to both ends of the MoS_2 fibers to ensure stable electrical contacts. The *I–V* characteristics were measured using a source-measure unit (Keithley 2401, Tektronix) equipped with a probe station (ST-500-1-4CX, Janus). To evaluate the sensing performance, *I–V* curves were recorded under various concentrations (mM range) of NaCl, KCl, NH_4Cl, and lactic acid, which were selected to simulate key components of human sweat. Prior to the application of real sweat, the real-time current response was monitored using artificial sweat, confirming that the response varied with the sweat volume.

Electrochemical measurements were conducted using a potentiostat/galvanostat/zero-resistance ammeter (Reference 3000, Gamry Instruments) with a standard three-electrode configuration, which consisted of a Pt CE and a Ag/AgCl RE. The CV curves were acquired in 0.1 mM solutions of NaCl, KCl, NH_4Cl, and lactic acid at scan rates ranging from 5 to 200 mV/s. The potential response was monitored by incrementally increasing the concentration of each analyte in deionized water.

4.5 | Electromechanical Pressure Sensing Measurements

To investigate the electromechanical response of the MoS_2/PLA composite fibers, pressure sensing tests were conducted. The fiber sensor was placed on a rigid substrate and a controlled vertical force was applied using a force gauge (DST-50N, Imada). The real-time current variations were monitored using a source meter (Keithley 2401, Tektronix) while applying cyclic force loads ranging from 1 to 5 N. The sensing performance was evaluated by calculating the relative change in current as a function of the applied force.

4.6 | Evaluation of the Heat Retention Properties of MoS_2 Fiber-Integrated Rings

To evaluate the thermal insulation performance of the MoS_2 fibers in a wearable form, a ring-shaped textile device was fabricated. Specifically, multiple strands of MoS_2 fibers were embedded into a long strip of commercial fabric to form a core–sheath structure. The temperature variations were monitored using an IR thermal camera. Thermal images were captured under three conditions to assess heat retention: before wearing the ring (baseline), while wearing the ring, and immediately after removing the ring following 5 min of physical exercise.

4.7 | Real Sweat Measurements

Sweat samples were obtained from healthy volunteers who provided informed consent. The collected samples were immediately used for sensing tests without any additional treatment. The electrical current was measured while varying the volume of sweat applied to evaluate the quantitative response. Furthermore, to investigate the sensing behavior during the drying process, real-time current variations were continuously monitored following the application of a single droplet of sweat and until reaching complete evaporation. All experiments involving human sweat samples were performed in accordance with the guidelines and regulations approved by the Institutional Review Board (IRB) of DGIST (Approval No. DGISTIRB-202512-002). Informed consent was obtained from all human subjects prior to the experiments.

Author Contributions

Bong Hoon Kim: conceptualization (lead), funding acquisition (lead), project administration (lead), writing – original draft (lead). **Jun Hyun Park:** data curation (equal), methodology (equal), supervision (equal), writing– original draft (equal). **Jae Woo Park:** formal analysis (equal), methodology (equal), writing – original draft (equal). **Min Seok Choi:** methodology (equal), validation (equal), visualization (equal). **Sang Uk Pang:** methodology (supporting), software (supporting). **Jun Seok Choe:** methodology (supporting), validation (supporting). **Tae Sang Yu:** methodology (supporting), software (supporting). **Kyung-In Jang:** supervision (supporting), visualization (supporting). **Jin-Tae Kim:** project administration (lead), writing – original draft (lead). **Ha Uk Chung:** software (lead), writing – original draft (lead). **Jang Hwan Kim:** investigation (lead), supervision (lead), writing – original draft (lead), writing – review and editing (lead).

Acknowledgments

This work was supported by the National Research Foundation of Korea (NRF) grant funded by the Korea government (MSIT) (grant no. RS-2024-00406240); the Basic Science Research Program through the National Research Foundation of Korea (NRF) funded by the Ministry of Education (grant no. RS-2025-25420118); the Nano & Material Technology Development Program through the National Research Foundation of Korea (NRF) funded by Ministry of Science and ICT (grant no. RS-2025-25442577); a grant of Korean ARPA-H Project through the Korea Health Industry Development Institute (KHIDI), funded by the Ministry of Health & Welfare, Republic of Korea (grant no. RS-2025-25454431); and the National Research Foundation of Korea (NRF) grant funded by the Korea government (MSIT) (grant no. RS-2025-00513522).

Funding

This work was supported by Ministry of Science and ICT, South Korea (RS-2024-00406240, RS-2025-25420118, RS-2025-25442577, RS-2025-00513522), Ministry of Health and Welfare (RS-2025-25454431).

Conflicts of Interest

The authors declare no conflicts of interest.

Data Availability Statement

The data that support the findings of this study are either provided in the source data or are available from the corresponding author upon reasonable request.

References

1. F. Gao, C. Liu, L. Zhang, et al., "Wearable and Flexible Electrochemical Sensors for Sweat Analysis: A Review," *Microsystems & Nanoengineering* 9, no. 1 (2023): 1, https://doi.org/10.1038/s41378-022-00443-6.

2. J. Heikenfeld, A. Jajack, B. Feldman, et al., "Accessing Analytes in Biofluids for Peripheral Biochemical Monitoring," *Nature Biotechnology* 37, no. 4 (2019): 407–419, https://doi.org/10.1038/s41587-019-0040-3.

3. Z. Sonner, E. Wilder, J. Heikenfeld, et al., "The Microfluidics of the Eccrine Sweat Gland, including Biomarker Partitioning, Transport, and Biosensing Implications," *Biomicrofluidics* 9, no. 3 (2015): 031301, https://doi.org/10.1063/1.4921039.

4. Y. Pang, Z. Yang, Y. Yang, and T. L. Ren, "Wearable Electronics Based on 2D Materials for Human Physiological Information Detection," *Small* 16, no. 15 (2020): 1901124, https://doi.org/10.1002/smll.202070083.

5. H. Y. Y. Nyein, L.-C. Tai, Q. P. Ngo, et al., "A Wearable Microfluidic Sensing Patch for Dynamic Sweat Secretion Analysis," *ACS Sensors* 3, no. 5 (2018): 944–952, https://doi.org/10.1021/acssensors.7b00961.

6. W. Jia, A. J. Bandodkar, G. Valdés-Ramírez, et al., "Electrochemical Tattoo Biosensors for Real-Time Noninvasive Lactate Monitoring in Human Perspiration," *Analytical Chemistry* 85, no. 14 (2013): 6553–6560, https://doi.org/10.1021/ac401573r.

7. T. Guinovart, A. J. Bandodkar, J. R. Windmiller, F. J. Andrade, and J. Wang, "A Potentiometric Tattoo Sensor for Monitoring Ammonium in Sweat," *The Analyst* 138, no. 22 (2013): 7031–7038, https://doi.org/10.1039/c3an01672b.

8. S. Jadoon, S. Karim, M. R. Akram, et al., "Recent Developments in Sweat Analysis and Its Applications," *International Journal of Analytical Chemistry* 2015, no. 1 (2015): 164974, https://doi.org/10.1155/2015/164974.

9. K. Sato, W. Kang, K. Saga, and K. Sato, "Biology of Sweat Glands and Their Disorders. I. Normal Sweat Gland Function," *Journal of the American Academy of Dermatology* 20, no. 4 (1989): 537–563, https://doi.org/10.1016/s0190-9622(89)70063-3.

10. S. Emaminejad, W. Gao, E. Wu, et al., "Autonomous Sweat Extraction and Analysis Applied to Cystic Fibrosis and Glucose Monitoring Using a Fully Integrated Wearable Platform," *Proceedings of the National Academy of Sciences* 114, no. 18 (2017): 4625–4630, https://doi.org/10.1073/pnas.1701740114.

11. J. J. Kim, Y. Wang, H. Wang, S. Lee, T. Yokota, and T. Someya, "Skin Electronics: Next-Generation Device Platform for Virtual and Augmented Reality," *Advanced Functional Materials* 31, no. 39 (2021): 2009602, https://doi.org/10.1002/adfm.202170286.

12. T. R. Ray, J. Choi, A. J. Bandodkar, et al., "Bio-Integrated Wearable Systems: A Comprehensive Review," *Chemical Reviews* 119, no. 8 (2019): 5461–5533, https://doi.org/10.1021/acs.chemrev.8b00573.

13. W. Gao, S. Emaminejad, H. Y. Y. Nyein, et al., "Fully Integrated Wearable Sensor Arrays for Multiplexed In Situ Perspiration Analysis," *Nature* 529, no. 7587 (2016): 509–514, https://doi.org/10.1038/nature16521.

14. J. Song, I. Jung, and H. Kim, "Non-Invasive Glucose Measurement Using Electric Field and Temperature Sensor," *Journal of Sensor Science and Technology* 34, no. 5 (2025): 549–554, https://doi.org/10.46670/jsst.2025.34.5.549.

15. E. S. Lim, S. H. Lee, J. Choi, Y. J. Lim, and H. U. Chung, "Advances in Skin-Interfaced Wireless Physiological Monitoring Systems," *Journal of Sensor Science and Technology* 34, no. 5 (2025): 458–472, https://doi.org/10.46670/jsst.2025.34.5.458.

16. A. Childs, B. Mayol, J. A. Lasalde-Ramírez, Y. Song, J. R. Sempionatto, and W. Gao, "Diving into Sweat: Advances, Challenges, and Future Directions in Wearable Sweat Sensing," *ACS Nano* 18, no. 36 (2024): 24605–24616, https://doi.org/10.1021/acsnano.4c10344.

17. J. Min, J. Tu, C. Xu, et al., "Skin-Interfaced Wearable Sweat Sensors for Precision Medicine," *Chemical Reviews* 123, no. 8 (2023): 5049–5138, https://doi.org/10.1021/acs.chemrev.2c00823.

18. Z. Wang, H. Li, Z. Tang, et al., "Hydrogel Electrolytes for Flexible Aqueous Energy Storage Devices," *Advanced Functional Materials* 28, no. 48 (2018): 1804560, https://doi.org/10.1002/adfm.201804560.

19. J. H. Park, J. H. Kim, S. E. Lee, et al., "2D MoS_2 Helical Liquid Crystalline Fibers for Multifunctional Wearable Sensors," *Advanced Fiber Materials* 6 (2024): 1–12, https://doi.org/10.1007/s42765-024-00450-4.

20. W. He, C. Wang, H. Wang, et al., "Integrated Textile Sensor Patch for Real-Time and Multiplex Sweat Analysis," *Science Advances* 5, no. 11 (2019): eaax0649, https://doi.org/10.1126/sciadv.aax0649.

21. G. Wang, B. Wu, Q. Li, et al., "Active Transportation of Liposome Enhances Tumor Accumulation, Penetration, and Therapeutic Efficacy," *Small* 16, no. 44 (2020): 2004172, https://doi.org/10.1002/smll.202004172.

22. T. Shi, R. Wang, Z. Wu, Y. Sun, J. An, and Q. Liu, "A Review of Resistive Switching Devices: Performance Improvement, Characterization, and Applications," *Small Structures* 2, no. 4 (2021): 2000109, https://doi.org/10.1002/sstr.202000109.

23. J. Kim, I. Jeerapan, S. Imani, et al., "Noninvasive Alcohol Monitoring Using a Wearable Tattoo-Based Iontophoretic-Biosensing System," *ACS Sensors* 1, no. 8 (2016): 1011–1019, https://doi.org/10.1021/acssensors.6b00356.

24. A. Koh, D. Kang, Y. Xue, et al., "A Soft, Wearable Microfluidic Device for the Capture, Storage, and Colorimetric Sensing of Sweat," *Science Translational Medicine* 8, no. 366 (2016): 366ra165–366ra165, https://doi.org/10.1126/scitranslmed.aaf2593.

25. S. B. Kim, K. Lee, M. S. Raj, et al., "Soft, Skin-Interfaced Microfluidic Systems with Wireless, Battery-Free Electronics for Digital, Real-Time Tracking of Sweat Loss and Electrolyte Composition," *Small* 14, no. 45 (2018): 1802876, https://doi.org/10.1002/smll.201802876.

26. A. Martín, J. Kim, J. F. Kurniawan, et al., "Epidermal Microfluidic Electrochemical Detection System: Enhanced Sweat Sampling and Metabolite Detection," *ACS Sensors* 2, no. 12 (2017): 1860–1868, https://doi.org/10.1021/acssensors.7b00729.

27. L. B. Baker, J. B. Model, K. A. Barnes, et al., "Skin-Interfaced Microfluidic System with Personalized Sweating Rate and Sweat Chloride Analytics for Sports Science Applications," *Science Advances* 6, no. 50 (2020): eabe3929, https://doi.org/10.1126/sciadv.abe3929.

28. X. Xuan, C. Chen, A. Molinero-Fernandez, et al., "Fully Integrated Wearable Device for Continuous Sweat Lactate Monitoring in Sports," *ACS Sensors* 8, no. 6 (2023): 2401–2409, https://doi.org/10.1021/acssensors.3c00708.

29. X. Li, X. He, X. Yang, G. Tian, C. Liu, and T. Xu, "A Wearable Sensor Patch for Joule-Heating Sweating and Comfortable Biofluid Monitoring," *Sensors and Actuators B: Chemical* 419 (2024): 136399, https://doi.org/10.1016/j.snb.2024.136399.

30. S. E. Lee, J. Seo, S. Kim, et al., "Reversible Solar Heating and Radiative Cooling Devices via Mechanically Guided Assembly of 3D Macro/Microstructures," *Advanced Materials* 36, no. 39 (2024): 2400930, https://doi.org/10.1002/adma.202470309.

31. H. J. Jin, J. Seo, H. U. Chung, et al., "Development of 3D Reversible Smart Energy-Saving Devices for Adaptive Energy Management," *Advanced Materials* 37 (2025): 2507682, https://doi.org/10.1002/adma.70848.

32. Z. Li, B. Wang, J. Lu, et al., "Highly Stretchable, Self-Healable, and Conductive Gelatin Methacryloyl Hydrogel for Long-Lasting Wearable Tactile Sensors," *Advanced Science* 12 (2025): e02678, https://doi.org/10.1002/advs.202502678.

33. A. Miyamoto, S. Lee, N. F. Cooray, et al., "Inflammation-Free, Gas-Permeable, Lightweight, Stretchable on-Skin Electronics with Nanomeshes," *Nature Nanotechnology* 12, no. 9 (2017): 907–913, https://doi.org/10.1038/nnano.2017.125.

34. D.-H. Kim, N. Lu, R. Ma, et al., "Epidermal Electronics," *Science* 333, no. 6044 (2011): 838–843, https://doi.org/10.1126/science.1206157.

35. M. Kaltenbrunner, T. Sekitani, J. Reeder, et al., "An Ultra-Lightweight Design for Imperceptible Plastic Electronics," *Nature* 499, no. 7459 (2013): 458–463, https://doi.org/10.1038/nature12314.

36. M. J. Ahn, G. Yoo, S. M. Kim, et al., "Soft Conductive Nanocomposites for Skin-Interfaced Physiological Monitoring," *Journal of Sensor Science and Technology* 34, no. 5 (2025): 473–487, https://doi.org/10.46670/jsst.2025.34.5.473.

37. A. K. Metya and C. K. Das, "Electrolyte under Molybdenum Disulfide Surfaces: Molecular Insights on Structure and Dynamics of Water," *Langmuir* 40, no. 7 (2024): 3540–3548, https://doi.org/10.1021/acs.langmuir.3c03184.

38. Z. Weng, J. Zhu, L. Lu, Y. Ma, and J. Cai, "Regulation of the Electric Double-Layer Capacitance of MoS_2/Ionic Liquid by Carbon Modification," *Journal of Applied Electrochemistry* 53, no. 4 (2023): 689–703, https://doi.org/10.1007/s10800-022-01802-x.

39. S. C. Lau and C. L. Bilodeau, "Effect of Monovalent Cations on the Structure and Dynamics of Multimodal Chromatographic Surfaces," *Langmuir* 40, no. 13 (2024): 6694–6702, https://doi.org/10.1021/acs.langmuir.3c03294.

40. T. Lim, Y. Kim, S. M. Jeong, et al., "Human Sweat Monitoring Using Polymer-Based Fiber," *Scientific Reports* 9 (2019): 17294, https://doi.org/10.1038/s41598-019-53677-2.

41. X. Wang, Y. Liu, Z. Sun, J. Wang, J. Xu, and M. Yang, "A Thread-Based Wearable Sweat Nanobiosensor," *Biosensors and Bioelectronics* 188 (2021): 113270, https://doi.org/10.1016/j.bios.2021.113270.

42. D. Jia, T. Yang, K. Wang, et al., "Facile in-Situ Synthesis of $Ti_3C_2T_x$/TiO_2 Nanowires toward Simultaneous Determination of Ascorbic Acid, Dopamine and Uric Acid," *Journal of Alloys and Compounds* 985 (2024): 173392, https://doi.org/10.1016/j.jallcom.2023.173392.

43. Y. Lv, T. Yang, E. Wang, et al., "Hou High-Sensitivity PZT-OV/$Ti_3C_2T_x$/PVDF Piezoelectric Fiber for Self-Powered Vital Signs Monitoring," *eScience* (2026): 100530, https://doi.org/10.1016/j.esci.2026.100530.

44. T. Yang, D. Jia, B. Xu, et al., "Textured $CsPbI_3$ Nanorods Composite Fibers for Stable High Output Piezoelectric Energy Harvester," *EScience* 4 (2024): 100273, https://doi.org/10.1016/j.esci.2024.100273.

45. Y. Xue, T. Yang, Y. Zheng, et al., "Heterojunction Engineering Enhanced Self-Polarization of PVDF/$CsPbBr_3$/$Ti_3C_2T_x$ Composite Fibers," *Advanced Science* 10 (2023): 2300650, https://doi.org/10.1002/advs.202300650.

46. S. Biccai, C. S. Boland, D. P. O'Driscoll, et al., "Negative Gauge Factor Piezoresistive Composites Based on Polymers Filled with MoS_2 Nanosheets," *ACS Nano* 13, no. 6 (2019): 6845–6855, https://doi.org/10.1021/acsnano.9b01613.

47. E. Bilotti Dong, H. Zhang, C. S. Boland, and D. G. Papageorgiou, "High Performing Piezoresistive MoS_2/Epoxy Strain Sensors for Structural Health Monitoring," *Polymer* 309 (2024): 127449, https://doi.org/10.1016/j.polymer.2024.127449.

Supporting Information

Additional supporting information can be found online in the Supporting Information section. **Supporting Fig. S1:** XPS spectra recorded for the raw bulk MoS_2 powder used as the starting material. The core level spectra of (left) Mo 3d and (right) S 2p exhibit the characteristic peaks of the semiconducting 2H phase before the exfoliation process. **Supporting Fig. S2:** Normalized electrical responses of the MoS_2/PLA composite fiber to electrolytes (NaCl, KCl, NH_4Cl and lactic acid) as a function of concentration. **Supporting Fig. S3:** I–V characteristics of the MoS_2/PLA composite fiber sensor measured under mixed electrolyte and electrolyte–metabolite conditions: (a) mixed NaCl/KCl electrolytes with varying ionic ratios, and (b) electrolyte–metabolite coexistence systems consisting of NaCl 45 mM/KCl 5 mM with lactic acid at different concentrations (5 mM and 20 mM). **Supporting Fig. S4:** I–V characteristics of the MoS_2/PLA composite fiber sensor measured at different pH values (pH 4.0, 5.5, and 7.5) in artificial sweat containing (a) NaCl 45 mM and (b) NaCl 45 mM, glucose 0.1 mM, and urea 25 mM. **Supporting Fig. S5:** Results of re-measurement of the cyclic sweat droplet-drying current response of a MoS_2/PLA composite fiber sensor using artificial sweat. **Supporting Fig. S6:** Results of re-measurement of the cyclic sweat droplet-drying current response of a MoS_2/PLA composite fiber sensor after one month of storage. **Supporting Fig. S7:** Photograph of the MoS_2/PLA composite fiber bent into a U-shaped configuration and normalized resistance change ($\Delta R/R_0$) of the MoS_2/PLA composite fiber as a function of repeated bending cycles. **Supporting Fig. S8:** Mechanical robustness and pressure-sensing stability of the MoS_2/PLA composite fiber. (a) Current–voltage (I–V) characteristics of three independent fiber samples before and after the application of a 10 N external load. (b) Comparison of the normalized resistance change for the three samples under 10 N loading, demonstrating device-to-device consistency. (c) Repeatable resistance response over five consecutive loading-unloading cycles at a moderate pressure of 5 N. **Supporting Table S1:** Quantitative comparison of analytical performance between the proposed MoS_2/PLA composite fiber and recently reported nanomaterial-based sensors.